HHS Public Access

Author manuscript

Nat Biomed Eng. Author manuscript; available in PMC 2023 November 16.

Published in final edited form as:

Nat Biomed Eng. 2023 October ; 7(10): 1229–1241. doi:10.1038/s41551-023-01098-y.

Synchronized wearables for the detection of hemodynamic states via electrocardiography and multispectral photoplethysmography

Daniel Franklin[1,2,&,*], **Andreas Tzavelis**[3,4,5,&], **Jong Yoon Lee**[6], **Ha Uk Chung**[6], **Jacob Trueb**[5], **Hany Arafa**[4,5], **Sung Soo Kwak**[5], **Ivy Huang**[5,7], **Yiming Liu**[8], **Megh Rathod**[1,2], **Jonathan Wu**[1,2], **Haolin Liu**[1,2], **Changsheng Wu**[7], **Jay Pandit**[9], **Faraz S. Ahmad**[10], **Patrick M. McCarthy**[11], **John A. Rogers**[4,5,7,12,*]

[1]Institute of Biomedical Engineering, University of Toronto, Toronto, ON, M5S 3E2, Canada

[2]Ted Rogers Centre for Heart Research, Peter Munk Cardiac Centre, University Health Network, Toronto, ON, M5G 1M1, Canada

[3]Medical Scientist Training Program, Feinberg School of Medicine, Northwestern University, Chicago, IL 60611, USA

[4]Department of Biomedical Engineering, McCormick School of Engineering, Northwestern University, Evanston, IL 60208, USA.

[5]Querrey Simpson Institute for Bioelectronics, Northwestern University, Evanston, IL 60611, USA.

[6]Sibel Health, Niles, IL 60714, USA.

[7]Department of Materials Science and Engineering, McCormick School of Engineering, Northwestern University, Evanston, IL 60208, USA.

[8]Department of Electrical and Computer Engineering, McCormick School of Engineering, Northwestern University, Evanston, IL 60208, USA.

[9]Scripps Research Translational Institute, San Diego, CA

[10]Division of Cardiology, Department of Medicine, Bluhm Cardiovascular Institute, Northwestern University, Chicago, IL 60611, USA

[*]Corresponding authors, dan.franklin@utoronto.ca; jrogers@northwestern.edu.

[&]These authors contributed equally

Author contributions

A.T. and D.F. conceptualized the work. A.T., D.F., J.Y.L., H.A., J.T., H.U.C., S.S.K. and C.W. developed the methodology. A.T., D.F., H.A., Y.L., I.H., M.R., J.W., H.L. and J.P. performed experiments. A.T. and D.F. visualized data. A.T., D.F. and J.A.R acquired funding. J.P., F.S.A., P.M.M. and J.A.R. supervised the project. A.T. and D.F. wrote the manuscript. A.T., D.F., J.P., F.S.A. and J.A.R. edited the manuscript.

Competing interests

J.Y.L., H.U.C. and J.A.R. own equity in Sibel Health and hold patents (US20210361165A1, USA 2021 pending; US20210386300A1, USA 2021 pending; WO2023043866A1, WIPO 2023) associated with this company. The other authors declare no competing interests.

Code availability

Code used for analysis and to produce figures is also available upon reasonable request to the corresponding authors; however, implementations of methods described in the text exist in public repositories described in the data analysis section and in referenced work.

[11]Division of Cardiac Surgery, Department of Surgery, Bluhm Cardiovascular Institute, Northwestern University, Chicago, IL 60611, USA

[12]Department of Neurological Surgery, Feinberg School of Medicine, Northwestern University, Chicago, IL 60611, USA.

Abstract

Cardiovascular health is typically monitored by measuring blood pressure. Here we describe a wireless on-skin system consisting of synchronized sensors for chest electrocardiography and peripheral multispectral photoplethysmography for the continuous monitoring of metrics related to vascular resistance, cardiac output and blood-pressure regulation. We used data from the sensors to train a support-vector-machine model for the classification of hemodynamic states (resulting from exposure to heat or cold, physical exercise, breath holding, performing the Valsalva maneuver or from vasopressor administration during post-operative hypotension) that independently affect blood pressure, cardiac output and vascular resistance. The model classified the hemodynamic states on the basis of an unseen subset of sensor data for 10 healthy individuals, 20 patients with hypertension undergoing hemodynamic stimuli and 15 patients recovering from cardiac surgery, with an average precision of 0.878 and an overall area under the receiver operating characteristic curve of 0.958. The multinodal sensor system may provide clinically actionable insights into hemodynamic states for use in the management of cardiovascular disease.

Assessment of cardiopulmonary function is essential in the diagnosis and management of physiologic insufficiency and decompensation in life-threatening conditions such as circulatory shock[1,2]. This hemodynamic evaluation involves the assessment of volume status (distributive), cardiac function (cardiogenic) and vascular tone (vasogenic) factors to target treatment plans[3,4]. The simplest methods rely on physical exams, vital signs and blood pressure (BP) measurements[5]. In most cases, however, these assessments are intermittently captured and provide only a partial view of hemodynamic status, especially when signs change rapidly, overlap, or are obscured by physiologic compensation[6,7].

Blood pressure is the product of the heart's ability to generate blood flow, cardiac output (CO), against the resistance of the body's vascular beds, systemic vascular resistance (SVR)[7]. Dynamic changes in the balance of CO and SVR may mask changes in BP, complicating the identification of abnormal states that require intervention[6]. In complex and severe cases that are unresponsive to first-line treatments, guideline-directed[1] management still recommends invasive hemodynamic monitoring, including arterial pressure catheters for continuous BP measurement[8] and pulmonary artery catheterization for the estimation of CO[9]. Estimates of SVR follow from the division of mean arterial BP by CO. Currently, these invasive measurements are not recommended for patients outside of critical care owing to substantial infection or trauma risks[10], the requirement of specially trained personnel and the physically limiting nature of these interventions. Studies in patients with selected heart failure have shown that ambulatory measurements from implantable pulmonary artery pressure sensors reduce hospitalizations[11,12]; however, the most recent guideline consensus remains uncertain on these benefits[1].

Recent advances in wireless, skin-interfaced sensor technologies enable the continuous collection of critical health parameters that greatly improve the ability to monitor patient status non-invasively, continuously and remotely[13,14]. The latest devices support measurements of heart rate (HR), respiration rate (RR), physical activity and blood oxygenation, in many cases with regulatory approvals for use in the hospital and at home, across a wide range of age groups[15–20]. Unfortunately, the estimation of BP using wearable cuffless technology remains challenging[21–25]. The most common approach to estimating blood pressure using wearable technology is through pulse wave velocity (PWV), which relates the stiffness of the arteries to driving pressure through empirical calibrations based on the Moens–Korteweg and Hughes equations[26–29]. PWV can be measured non-invasively across a known distance through the time delay between the electrocardiogram (ECG) R-peak or mechano-acoustic measurements of aortic valvular openings and specific features in peripheral photoplethysmogram (PPG) waveforms (known as pulse arrival time (PAT) and pulse transit time (PTT), respectively). Although this approach has shown promise, it does not account for dynamic changes in the underlying vessel bed that can occur during conditions such as physical exercise[28,30,31], administration of vasoactive pharmaceuticals[32,33], variations in ambient temperature[34,35], circadian rhythms[36] and other natural activities. PWV can be highly correlated with HR, and care must be taken to evaluate PWV measurements under variable conditions where HR and BP are not highly correlated to prevent confounding[37,38]. In addition, efforts pursuing non-invasive methods of continuous CO estimation include impedance cardiography[39] and pulse waveform/pulse pressure analysis[40,41], but these suffer from similar assumptions, empirically derived models, confounders or tedious and invasive calibration requirements similar to PWV measurements.

Beyond BP and CO, SVR measurements are difficult to obtain directly. However, recent work[42–45] suggests that arteriolar state, the primary factor determining vascular resistance, can be captured by exploiting the wavelength-dependent penetration depth of light into the skin. Shorter-wavelength blue-green light interacts primarily with near-surface capillaries, whereas red-infrared light interacts with larger arteries in the subdermal plexus. Thus, by deconvolving arterial and capillary pulsations, it is possible to quantify pulse-wave propagation from the subdermal plexus, through arterioles, to near-surface capillaries. This arteriolar pulse propagation time, herein termed ‘MW delay’ owing to the multiwavelength method of extraction, is modulated by the variable arteriolar diameter elicited by constriction or dilation and is thus related to local vascular resistance.

Tracking these factors continuously and remotely with discrete wearables provides a promising path towards personalized, outcome-oriented[14] healthcare management. Beyond healthcare, wireless non-invasive hemodynamic measurements may have implications in physical performance assessments such as exercise readiness and recovery[46–49], or cognitive stress management[50]. These considerations suggest that a multimodal approach is favorable over a single-parameter model to disentangle complex physiological interactions as the body experiences hemodynamic changes.

Here we build on these concepts to develop a multinodal and wireless skin-interfaced system capable of continuous hemodynamic classification within the BP, CO and SVR coordinate

space. The approach combines a peripherally worn multiwavelength and multispatial photoplethysmography (MWPPG) sensor with a chest-worn device that captures signals related to cardiac activity[51]. By uniting conventional time-synchronized PAT measurements, a correlate of local vascular resistance through MW delay, and HR, this wearable system can measure and classify physiological changes associated with specific hemodynamic states, thus delivering clinically actionable information[14]. Pilot studies revealed the impact of short-term hemodynamic stimuli in healthy participants and in patients with hypertension through cold pressor tests, breath holds, Valsalva maneuvers, exercise and full-body heat exposure, as well as longer-term effects of pharmacological intervention during post-surgical recovery within a cardiothoracic intensive care unit. These hemodynamics-modulating activities elicit disparate responses in BP/SVR/CO, where the heart both drives and reacts to conditions throughout a full range of realistic natural scenarios.

Results

The hemodynamic monitoring system introduced here consists of a central, chest-worn sensor for ECG and seismocardiogram (SCG) measurements along with a peripheral MWPPG unit for simultaneous acquisition of multimodal cardiac signals. Fig. 1a showcases the ECG/SCG device and peripheral MWPPG communicating wirelessly to a central control module with custom software that coordinates time synchronization and manages data transfer through the Bluetooth low-energy (BLE) protocol. The advantage of this combined approach is that both arterial PWV, corresponding to systemic factors, and arteriolar PWV, corresponding to local vascular dynamics, can be extracted simultaneously (Fig. 1b). Arterial stiffness and BP primarily determine the systemic PWV, measured by PAT, while the arteriolar resistance primarily determines the arteriolar PWV, measured by MW delay. Fig. 1c outlines key clinical entities on the BP vs peripheral vascular resistance axis relative to the resting state. Even with perfect measurement, BP alone cannot differentiate these conditions—a multiparameter approach is required. By measuring arteriolar PWV in addition to systemic PWV and HR, it may be possible to disentangle these states.

Device design

The combined central-peripheral system uses a BLE-enabled system-on-a-chip (SoC) to control data collection and local data storage, and to ensure inter-device time synchronization and coordinated data transfer. The chest device, which extends designs reported previously for neonatal monitoring[51], incorporates an analogue differential amplifier-filter with filters tuned to the 0.5 Hz–80 Hz range for ECG measurements, a temperature sensor and a triaxial accelerometer that simultaneously measures SCG, core body motion, vocal processes and physical activity[52].

The peripheral device represents a unique enabling component of this system. This technology incorporates the same temperature sensor and accelerometer as the chest device for rejecting motion artefacts, determining orientation and recording physical activity. The key feature is a multispectral photodiode and linear array of light emitting diodes (LEDs) that emit across the visible and near-infrared region of the spectrum. Fig. 1d shows an exploded view that highlights these components, along with power management circuits

and subsystems for wireless charging of a small lithium-polymer battery, all separated into four mechanically isolated islands. The enclosure exploits a medical-grade silicone elastomer, with transparent windows for the four pairs of broadband white and near-infrared (NIR) LEDs and the multispectral photodiode (Fig. 1e). As illustrated in Fig. 1f–h and Supplementary Fig. 1, serpentine interconnects greatly improve device flexibility and mechanically isolate sensitive components from the battery, radio unit and other hardware. This flexibility also allows for multiple final device forms via folding of the circuit before encapsulation to improve the fidelity of operation and to allow use on nearly any part of the body, from central locations such as the forehead or ear, to peripheral locations such as fingers or the wrist (Fig. 1i). Signals provide information that is specific to the characteristics of regional vascular beds. For example, the earlobe and forehead yield rounded, capillary-like pulse waveforms without a strong dicrotic notch, while the finger produces sharp pulse onsets and a pronounced dicrotic notch presence due to increased wave reflections from branching arterial trees and larger vessels near the surface (Supplementary Fig. 2). In addition, low-frequency oscillations due to respiration can be seen overlayed with high-frequency oscillations due to the cardiac cycle.

Sensor modalities and analysis

The unique combination of broadband LEDs and a multispectral photodiode enables simultaneous spectroscopic measurements at 9 discrete wavelength bands in the visible–NIR range, shown in Fig. 1j and the illustration in Fig. 1k. Longer wavelengths of light have lower tissue absorption and thus travel deeper and further before absorption in tissue or capture by the photodiode[53]. Similarly, as the distance between the LED pairs and the multispectral photodiode increases, this effective penetration depth also increases. The multiwavelength approach emphasizes near-surface depth dependence. By contrast, the source-detector distance approach allows greater depths of penetration for longer wavelengths and is useful for spatially resolved tissue oxygenation measurements[54]. The source-detector distances are 3 mm, 6.5 mm, 10 mm and 13.5 mm.

For measurement of MW delay, the device operates at a fixed LED with source-detector distance of 3 mm and with six wavelengths of 480 nm, 515 nm, 555 nm, 590 nm, 680 nm and 900 nm, each with sampling rates of 100 Hz. These wavelengths penetrate the tissue to depths of approximately 0.3 mm, 0.4 mm, 0.5 mm, 1.0 mm, 2.3 mm and 1.8 mm, respectively, at 50% fluence[53]. The pulsations captured at each wavelength integrate contributions to the respective characteristic depths. Fig. 2a shows the high-level schematic for extracting arterial and capillary contributions from a wavelength depth-dependent mixture model[44], while Supplementary Fig. 3 covers this process at each step visually. All wavelengths contain a component of near-surface capillary pulsation, but yellow to NIR wavelengths also interact with arterioles and larger arteries. In each 5 s window, a principal component analysis (PCA) of the normalized 0.5 Hz–5 Hz bandpassed pulsatile waveforms at the two shallowest penetrating wavelengths, 480 nm and 515 nm, enables extraction of these near-surface, capillary-dominated pulsations. Calculation of the PCA at each window prevents gross motion artefacts or local variations in pulse morphology from influencing calculations in other windows, shown visually in Supplementary Fig. 3d,e. The first principal component of the short wavelengths represents pulsatile capillary blood

volume changes, while the second principal component arises from motion artefacts[44]. The first principal component of a separately calculated PCA of the normalized pulsatile waveforms at all available wavelengths extracts a superposed capillary-arterial pulse, from which the blue-green capillary pulse can be subtracted to isolate arterial pulsation. These arterial pulsations and capillary pulsations are cross-correlated with subsample interpolation. The delay at maximum correlation corresponds to the arteriolar pulse transit time (MW delay).

A block diagram of the combined sensor system is shown in Fig. 2b. The chest device captures single-lead ECG and triaxial accelerometry signals at sampling rates of 1 kHz and up to 3.3 kHz, respectively. The green wavelength data from the MWPPG device yields the pulse rate. These three signals (Fig. 2c) enable comparison of cardiac intervals known to be related to cardiovascular function, including the electromechanical delay/pre-ejection period (PEP), systolic/diastolic time intervals (left ventricular ejection time, LVET), pulse arrival time (PAT) and pulse transit time (PTT). Measurements of HR, RR and 2-wavelength (red–IR) pulse oxygenation (SpO_2) follow from MWPPG data, consistent with reference measurements as summarized in Fig. 2d–f. The pulsatile signal to noise ratio of the MWPPG device is 20.49 dB during hemodynamic pressors and is calculated in Supplementary Fig. 4.

Hemodynamic experiments

A set of experiments which elicit distinct hemodynamic responses within the BP-SVR-CO coordinate space and target separate BP regulatory mechanisms were chosen. Pilot studies with specific hemodynamic stimuli protocols produced data from healthy participants and patients with hypertension, with reference BP measurements provided by a volume-clamp-based continuous non-invasive arterial BP monitor. Examination of the effects of pharmaceutical modulation focuses on patients recovering in the cardiothoracic intensive care unit following mitral valve repair who required norepinephrine or epinephrine as standard clinical intervention in the immediate post-operative period in response to hypotension. Medical record data on medications, vital sign measurements and laboratory values provide reference information for these patients. Supplementary Table 1 displays characteristic changes relative to baseline across these experiments. Fig. 2a shows a representative dataset on a healthy participant during cycles of interleaved, short-term stimuli to modulate BP in contrasting ways: Valsalva maneuvers, cold pressor tests and breath holds. The presentation includes changes in HR, PAT and MW delay alongside reference measurements of BP, demonstrating measurement repeatability.

Valsalva

The Valsalva maneuver elicits a classical four-stage BP response[55] as thoracic pressure is increased, held and released. Because BP in this case is externally mediated and the heart reacts to baroreceptor stimulation, HR varies inversely with BP. PAT also exhibits an inverse response to BP as expected from theory[26,29,55,56]. However, the response does not track perfectly with BP probably due to uneven central-peripheral pressure differential among other vasomotor compensatory effects[55,56]. MW delay, in contrast, exhibits a variable increase during Valsalva phase II, which amplifies each repeated cycle associated with the time duration of the individual Valsalva maneuvers. Peripheral vasoconstriction is known to

occur in response to decreased pulse pressure[55,56]; the longer a Valsalva is held, the longer the body compensates for the decreased pulse pressure.

Cold pressor

Cold pressor challenges assess autonomic function, specifically sympathetic responses including vasoconstriction in the contralateral appendage[57]. These tests elicit a gradual increase in BP due to sympathetic stimulation of both the heart and peripheral vessels. This dynamic process involves a rapid increase in HR, followed by sustained oscillations throughout the challenge[58]. An initial rapid decrease in PAT correlates with a small sharp increase in BP, perhaps associated with bracing or initial shock. PAT then returns to values near the baseline, followed by a second smaller decrease near the final seconds of cold exposure. This behavior contrasts with the expected decrease in PAT correlated with the increase in BP, probably due to autonomic driving forces that modify both arterial properties and cardiac contractility. MW delay, on the other hand, exhibits a sharp increase, with oscillations that coincide with the period of cold exposure. Most importantly, these features exhibit a phase lead relative to the rise in BP, coinciding with the exposure to the cold-water bath. This suggests that vasoconstriction, not BP change, is indeed responsible for the increase in MW delay.

Breath hold

Breath holds include features of both intrathoracic pressure change, similar to the Valsalva maneuver, as well as peripheral vasoconstriction[59] due to sympathetic reactions to hypoxia and hypercapnia. This complex response elicits a gradual rise in BP, followed by a period of hypotension after breath release. The initial hold stage of this test leads o negligible changes in the HR and PAT. As the breath hold continues, however, it appears that MW delay changes remain in-phase with BP increase, contrary to the phase lead observations during the cold pressor test. Simultaneously, PAT remains constant until the BP begins to peak and the breath hold is released, exhibiting a phase lag to BP and MW delay. The minimum value of PAT during the breath holds coincides with a return of MW delay to baseline and a corresponding decrease in BP. This phasing behavior between PAT and MW delay with different driving forces of BP increase suggests a masking effect of arteriolar constriction on reflective-mode measurements of PAT or vice-versa.

Heat exposure

During prolonged heat exposure, the increase in temperature leads to peripheral vasodilation[60] and thus hypotension due to decreased peripheral resistance. To compensate, the HR increases, increasing CO to maintain BP. The experiments involve exposure of healthy participants to elevated temperatures using a personal, portable sauna chamber for 20 min. The decrease in BP and increase in arterial compliance would, based on the empirical theory referenced previously, lead to a corresponding increase in PAT consistent with reported studies based on applanation tonometry[61–63]. While this trend is modestly observed on initial exposure to heat, after profuse perspiration begins and BP decreases further around 10 min after entry into the sauna, the data from the system reported here and presented in Fig. 3b indicate that a consistent decrease in PAT is observed. The MW delay also moderately decreases in-phase with the PAT. As with the cold pressor test and breath

hold challenges, this finding suggests that arteriolar pulse transit time may modulate PAT measured via reflective-mode PPG.

Physical exercise

Exercise increases metabolic demand and thus induces a corresponding increase in CO through an increase in HR and contractility[64,65]. The result increases BP until the heat of increased metabolic demand begins to induce vasodilation. As shown in Fig. 3c, these processes lead to an immediate decrease in PAT and an increase in HR (12 min). Between 12 and 15 min, PAT exhibits an inverse relationship with BP, as expected by theory. At 15 min, the participant begins to perspire, and MW delay begins to decrease in response to vasodilation. BP also begins to fall from its peak, but PAT and HR do not exhibit any similar inflection points. The decrease in MW delay after this point appears to balance the expected increase in PAT with the decrease in BP. For some period after exercise is complete, the vasodilation inferred by low MW delay is maintained. Overall, HR and PAT exhibit a stronger correlation in this experiment than PAT and BP, while MW delay trends add independent information.

Post-surgical monitoring

Patients undergoing cardiothoracic surgery procedures can experience post-operative hypotension following cardiopulmonary bypass and surgical cardiac injury[66]. Vasoconstrictive medications, such as phenylephrine, epinephrine or norepinephrine delivered in the immediate post-operative period can help to maintain BP and prevent cardiogenic shock without stressing the heart. These medications increase end-organ perfusion by increasing peripheral resistance, corresponding to an increase in MW delay relative to baseline. The results in Fig. 4 illustrate these trends for a representative patient during administration of intravenous epinephrine following a surgical procedure. After initial rooming and assessment concludes that administration of epinephrine is appropriate, the medication is started and tapered as determined by regular clinical assessment and decision making. For the patient in Fig. 4, the initial MW delay was high and experienced a decline as epinephrine was withdrawn. In the following period, BP remains low for several hours, during which MW delay experiences a resurgence and remains elevated relative to the period of 11h after surgical closure, when BP recovers to pre-surgical levels and the patient has recovered from anesthesia.

Hemodynamic classification

Complex homoeostatic feedback loops connect BP and peripheral resistance[67]. Depending on external stimuli or patient conditions, the equilibrium point between induced and compensatory changes in BP and peripheral resistance can shift relative to a defined resting state. Fig. 5a shows a theoretical plot of expected clustering of hemodynamic states explored in this work relative to a central resting state. The four ‘core’ examples that delineate this BP vs resistance axis into quadrants relative to the resting state are (1) the cold pressor test and breath holding, which result in increased BP mediated by an increase in peripheral resistance associated with vasoconstriction, (2) physical exercise, which results in increased BP mediated by increases in cardiovascular stress and metabolic demand, while simultaneously decreasing peripheral resistance via vasodilation, (3) heat exposure

via sauna, which results in decreased BP mediated by decreases in peripheral resistance associated with vasodilation and (4) patients treated with post-surgical vasopressors in the setting of post-operative hypotension, where decreased BP is treated by medications which increase peripheral resistance. As illustrated by this plot, BP alone (horizontal axis) cannot distinguish all hemodynamic states. The pathophysiology that brings a patient into each of these quadrants is mediated by entirely different factors; identifying which quadrant a patient is in thus guides the choice of intervention to return to baseline.

Fig. 5b presents two-dimensional (2D) projections of all data collected during this study separated by color for each hemodynamic stimulus. Each projection is across sensor-measured data (HR, PAT and MW delay) as well as reference systolic and diastolic BP (SBP, DBP). Supplementary Video 1 shows the same sensor-measured quantities in a 3D scatterplot. Several important observations can be inferred from the plots in Fig. 5b as well as overall Pearson correlations expanded upon in Supplementary Fig. 5. First, the effect of the studied hemodynamic states on BP can be observed in the top-leftmost plot between SBP and DBP. While systolic and diastolic BP values are indeed highly correlated, some stimuli including active exercise and the Valsalva maneuvers exhibit more independence between SBP and DBP, conditions with substantial pulse pressure variation. The next row emphasizes that across all the studied hemodynamic states, low correlation between HR and BP is achieved. High correlation between HR and BP is a notable confounder in hemodynamic studies especially studies of PWV[38]. The following row further substantiates these findings, as PAT is not highly correlated with BP across all hemodynamic states but remains highly correlated with HR. The final row presents scatters of MW delay against the reference BPs and sensor derived metrics, showing little to no correlation, as expected of a metric independent of CO or BP.

These plots illustrate the segregation of MW delay and BP into discrete states similar to the theoretical peripheral resistance-BP axis. Fig. 5c plots the natural logarithm of the ratio of MW delay values to baseline measurements (fold change) against reference SBP, replicating the theoretical plot in Fig. 5a. MW delay reliably identifies states of high and low peripheral resistance, regardless of BP. The distributions of MW delay for each hemodynamic stimulus are shown in Fig. 5d via letter-value boxplots[68]. Brunner–Munzel[69] tests for stochastic equality in non-normal, unequal-variance samples were performed for each stimulus against the baseline distribution. Overall observations of the clustering of sensor-measured parameters by hemodynamic stimuli in Fig. 5b–d suggest that classification of various hemodynamic states is possible using sensor data alone without requiring direct measurements of absolute BP or SVR.

On the basis of visual inspection of the data in Fig. 5 and Supplementary Video 1, a simple support vector classifier using the radial basis function kernel was chosen to separate the hemodynamic classes. The approach involves training on 20% of data for each condition, leaving the remaining 80% for testing and explainability evaluation. Data were not shuffled and were instead kept in chronological order to avoid contamination of the test set with similar sample points of the same participant performing the same activity used to train the model. The test set is thus maximally independent of the data used for training. Short-term dynamic stimuli, such as the Valsalva maneuver, were removed for this analysis. Stimuli

were further grouped into classification states on the basis of their induced physiological response. Cold pressors and breath holds were combined into one group characterized by increased vascular resistance and BP, while sauna exposure and post exercise were combined into one group characterized by decreased vascular resistance and BP. Support vector classifiers were defined as binary classifiers; to apply to a multiclass model, a separate model must be trained to classify each pair of classes. In this case, ${}_5C_2 = 10$ models were individually trained on the same subset of data, with the overall prediction deriving from a simple majority vote across all the one-vs-one models.

Fig. 6a shows the confusion matrix of the overall trained model when applied to the 80% left-out test data. Confusion occurs to a small degree between states where vasodilation is expected, or between states where vasoconstriction is expected, but not across different vascular states. For instance, confusion between exercise and sauna can be explained by varying exercise intensity, or conversely, by the relatively high heart rates achieved in the sauna for some individuals. Confusion of cold pressor tests from baseline can be explained by some baseline measurements occurring in a cold environment, or by cold exposure causing a wave-like response[58] of vasoconstriction followed by vasodilation, which may vary substantially even with slight deviations in bath temperature[70]. This phenomenon, in addition to the previously noted phase lead in MW delay response and relative invariance in PAT, may explain confusion of this dynamic stimulus. Fig. 6b shows the receiver operating characteristic (ROC) curves for each hemodynamic state for the left-out test data. Individual class ROC curves were computed in the one-vs-rest binary method, while the micro-average ROC combined these results accounting for class imbalance for an overall score. The micro-average AUROC is 0.958. Precision-recall curves are shown in Fig. 6c, and the micro-averaged precision is 0.878. Supplementary Fig. 6 shows additional analysis repeating this training process on other folds to demonstrate model stability and generate an estimate of variance to the ROC curves.

Model interpretability and explainability is of critical importance in medical applications as models become increasingly complex[71]. SHapely Additive exPlanations (SHAP) are a unified method of generating interpretable feature importance for each prediction[72]. In Supplementary Fig. 7, we apply SHAP analysis to the trained support vector classifier model on up to 100 random examples of each hemodynamic class from the test set to generate an estimate of the importance of each input feature, MW delay, PAT or HR, in generating those predictions. MW delay contributes most towards predictions involving vasoconstriction. PAT, on the other hand, decreases considerably in vasodilation and is thus most helpful for prediction in those states. Overall, HR is the most important feature enabling identification of deviations from baseline, which is naturally in line with conventional clinical understanding.

Discussion

We have described a non-invasive multinodal and skin-interfaced wireless system for measurements of independent hemodynamic variables. The devices and subsequent classification method show promise in supplementing intermittent cuff-based home BP monitoring and invasive monitoring approaches currently reserved for patients with acute

decompensated heart failure[1]. The key technological advance is in the development of a multiwavelength device that mounts on a peripheral body location to measure a correlate of local vasoconstriction and dilation in arteriolar pulse transit time through MW delay. The time-synchronized operation with a chest unit that captures ECG and SCG waveforms leads to data streams with diverse informational content. Data collected under a variety of scenarios indicate that the system yields consistent and repeatable results for individuals and between participants over a large BP range. The largest and most predictable BP variability was elicited on healthy participants undergoing specific tasks, whereas inpatient participants were simply monitored during their clinical course without intervention beyond the standard of care.

Results show that BP alone is not able to delineate all studied hemodynamic states. We show that arteriolar PWV estimation provided by the MW delay measurement is associated with vasoconstriction and dilation, and that its addition to conventional non-invasive measurements of HR and systemic PAT contributes meaningfully towards enabling hemodynamic classification.

A main limitation of this pilot study is the relatively small number of participants. We were not able to explicitly disentangle variations in skin thickness, melanin content, tolerance to pain and exercise, and vascular responsiveness. Future work will include broader outcome-oriented studies in diverse populations, aimed at determining early-warning and treatment thresholds. In addition, the classification method incorporates only HR, PAT and MW delay. However, the sensor system enables the collection of additional hemodynamic parameters, such as pre-ejection period and left ventricular ejection time. The inclusion of these quantities may further extend the capabilities of classification and correlate with central cardiac function, including contractility[73] and ejection fraction[74].

Together, the wireless monitoring system and classification method provide objective information on the hemodynamic state of an individual beyond that of BP alone. The detection of underlying BP regulatory mechanisms is of critical importance in guiding clinical decision-making. With the ability to detect short-term hemodynamic responses to stimuli, medium-term compensatory responses and longer-term trends, these technologies may provide early-warning signs of hemodynamic decompensation warranting follow-up or intervention and help health-conscious individuals keep track of meaningful vascular-health parameters.

Methods

Device fabrication

Circuit design was performed on electronic design automation software (Eagle v.9.6.1, Autodesk) and outsourced for manufacturing on 4-layer flexible printed circuit board (fPCB) (PFC Flex). Key elements of the circuit include (1) a multispectral photodiode (AS7341, ams-OSRAM AG), (2) 4 pairs of broadband white LEDs and IR LEDs (L130–6580002011001, Lumileds and SFH 4043, OSRAM), (3) power management electronics (BQ2510A, Texas Instruments), (4) NFC charging components (tuned coil and rectifier) to enable wireless charging, (5) a triaxial accelerometer (LSM6DSL, STMicroelectronics), (6)

an 8 Gb NAND flash memory (MT29F8G08), (7) a Bluetooth low-energy system-on-a-chip (ISP1807, Insight SiP) and (8) passive components.

The circuit layout is shown in Supplementary Fig. 8. The devices consist of four separate islands connected via serpentine fPCB traces to maximize mechanical flexibility while providing structural support for rigid components.

Encapsulation

The fPCBs were folded along the serpentine interconnects, depending on the intended final form factor (long for finger wrapping or short for placement on other surfaces), followed by attachment of 50 mAh Li-Po batteries. 3D computer-aided-designed aluminum molds for the top (out-facing) and bottom (sensor-side) encapsulation were created using AutoCAD (Autodesk) and milled using CNC milling (Modela MDX-540, Roland). The molds were used to cast medical-grade silicone elastomer (Silbione 4420, Elkem) shells, colored with cyan or black, visible–NIR-spectrum opaque silicone paint (Silc Pig) with holes for the 4 LED pairs and photodiode (PD) on the bottom and white on top. On glass slides, the bottom LED-PD holes were filled with transparent silicone (Ecoflex 00–31 Near Clear, Smooth-On) to bind the sensor head to the bottom encapsulation layer. The opposing outer shell was filled with remaining Ecoflex and the two sides of the silicone shell, with the device in between, were pressed together using external clamps and allowed to cure, thereby creating a sealed enclosure. Supplementary Fig. 9 further details the encapsulation process. Supplementary Fig. 10 shows the effect of encapsulation on white LED emission efficiency and spectrum.

Adhesives

Depending on the experiment, the device was adhered to the skin using a laser-cut, medical-grade, dual-sided silicone-acrylate adhesive (2477p, 3M). For long-term wear or for mounting during physical exercise and sauna, the devices were adhered with medical-grade transparent film adhesive (Tegaderm, 3M) or secured around a finger with medical-grade self-adhering wraps (Coban, 3M).

Data recording and transfer

The devices are capable of both local storage of measurement data as well as real-time streaming of data to a tablet or other mobile device through BLE protocol. This external device also provides coordination of timestamping events when nearby. The devices can form a network of time-synchronized nodes using methods described previously[51]. Pre-programmed sleep–wake intervals can be implemented to save battery life where continuous recording is not required (Supplementary Fig. 11). Supplementary Video 2 shows a demonstration of the sensor system and app streaming of real-time data.

Short-term and medium-term blood pressure experiments

Pilot studies rely on healthy participants (n = 10, 8 male, 2 female, median age 28 yr, s.d. 2.5 yr) with repeated exposure (total number of sets) to a sauna (10), cold pressor (21), physical exercise (15), breath holding (15) and Valsalva maneuver (20). Additional analysis includes data from 20 patients with hypertension (10 male, 10 female, median age 69 yr, s.d. 14

yr) collected during regular clinical visits with repeated Valsalva maneuvers. Data from six different wavelength channels from MWPPG signals captured using the first pair of LEDs were captured during simultaneous reference measurements of BP using the continuous volume-clamp method (NOVA, Finapres Medical Systems). Participants wore a MWPPG sensor on their non-dominant hand, as well as an ECG/ SCG sensor on their chest for HR and PAT. Participants were asked to rest for 5 min to establish baseline measurements, then to perform a Valsalva maneuver for not longer than 15 s, followed by a period of rest and return to within 5 mmHg of baseline systolic BP. Then, each participant placed their dominant (non-sensor) hand in a bucket of cold water not colder than 4 °C for as long as they were comfortable but not longer than 1 min. This procedure was followed by a rest and return to within 5 mmHg of baseline systolic BP and then a period of breath holding for as long as the participant was comfortable. After another return to 5 mmHg of baseline systolic BP, the pressors were repeated two more times for consistency. Participants with hypertension were only asked to perform the Valsalva maneuver. Any test that did not elicit a systolic BP rise >15 mmHg was not included in subsequent analysis. Participants were not asked to repeat the experiment for any missed cycle. Healthy participants willing to participate in additional medium-term experiments were asked to return for exercise or sauna testing. The devices were affixed in the same locations as the short-term BP experiments. For the sauna test, following a 10-min period of rest to establish baseline measurements, participants sat in a portable sauna for 30 min (or until tolerated) at 50 °C, followed by 15 min of recovery. For the exercise test, following a 10-min period for baseline measurements, the participants physically exercised at a moderate rate until light sweating was elicited, held that intensity for 10 min, and then stopped exercise and recovered for 15 min.

Post-surgical monitoring

The study devices were affixed to 15 (8 male, 7 female, median age 61 yr, s.d. 11.4 yr) previously informed and consented patients upon completion of cardiothoracic surgery in the Northwestern Memorial Hospital cardiothoracic intensive care unit. Sensors were placed as soon as possible following rooming in the cardiothoracic intensive care unit without interrupting standard of care procedures. Information on demographics (height, weight, age, sex), relevant cardiac medical history, hemodynamic modulating medications and relevant vital signs and laboratory measurements were collected via pre-defined queries through the Northwestern Electronic Data Warehouse (EDW). Sensor data and EDW data were de-identified, linked only through a unique participant ID. Only participants with clinically noted post-surgical hypotension treated by vasoconstrictive medications (for example, epinephrine, norepinephrine, phenylephrine) were considered for classification (n = 4, 1 male, 3 female); however, all data with additional medications and interventions are available for further analysis.

Data exclusion

Datasets were planned to be excluded if measurements during the baseline resting period varied by more than ±10 mmHg, as this could indicate problems with reference measurements or underlying hemodynamic instability, which could confound responses to

stimuli. Patients who were not treated with vasoconstrictive medication in the immediate post-operative period were excluded from analysis.

Extreme values due to artefacts were also excluded on a physiological basis (for example, sudden HR spikes or drops of >50 bpm that could indicate missed peaks), or if measurement values were >6 s.d.s from others in that dataset.

Data analysis

Analysis of sensor data was performed in Python 3.10 using openly available packages including NumPy (1.23.5)[75], SciPy (1.9.3)[76], Pandas (1.5.1)[77], Scikit-learn (1.1.2)[78] and SHAP (0.41.0)[72], with visualization in matplotlib (3.6.0)[79] and seaborn (0.11.2)[80]. Hemodynamic state labelling was performed on reference BP measurements (Finapres for short to medium-term experiments, Cuff BP or arterial line BP for patients) in combination with experiment timelines or medical record medication administration and events where available. Alignment between sensor data and labelled reference sources was accomplished by matching the HR calculation from the sensor system and Finapres or medical record HR values, as well as induced signal perturbations in both data streams by tapping. In the final HR, PAT and MW delay data used for the Fig. 5 scatterplots and classification, a 5 s median window was applied to all measurements around every detected heartbeat after grouping by label. To control for inter-participant variability due to differences in limb length, arterial tree morphology and baseline vascular tone, each datapoint was baseline subtracted. Baseline corresponded to the median value captured as the participant remained seated at rest for 5 min and diastolic BP remained within an interval of ±10 mmHg. The median value of each calculated parameter during this time was subtracted from each remaining datapoint for that set.

Heart rate–pulse arrival time calculation

The green wavelength at the 515 nm channel of the MWPPG signal was used for further processing given its relative resistance to blood volume changes in deeper layers driven by motion artefacts[81,82]. The signal was bandpass filtered with a zero-phase fourth-order Butterworth filter with cut-offs at 0.5 Hz–5 Hz. The first derivative of the bandpass filtered signal was calculated and passed through an automatic multiscale peak-detector algorithm[83]. In some cases, the R-peak of the ECG signal was used to determine a search domain for complementary first-derivative pulse peaks in the PPG waveform. Complementary ECG R-peak and PPG first-derivative peak locations were subtracted to calculate PAT.

Pulse oximetry

Blood oxygenation was defined as the ratio of oxygenated hemoglobin to total hemoglobin concentrations (c) in the following formula:

$$SpO_2 = \frac{c_{HbO_2}}{c_{HbO_2} + c_{Hb}} \times 100\%$$

Oxygenated hemoglobin has a local peak absorbance in the infrared range, roughly at 940 nm. A local minimum in absorbance occurs at roughly 680 nm, a wavelength where

deoxygenated hemoglobin absorbs more strongly. The wavelengths of 900 nm and 680 nm were used for analysis of SpO_2 in this study. Relative changes in reflected light intensity with frequencies between 0.5–10 Hz correspond to pulsatile signals that result from changes in blood volume changes. The time-independent part of the signal corresponds to light reflected from the bulk tissue. The quantity R, known as the ratio of ratios, is inversely related to SpO_2,

$$R = \frac{Pulse_{680nm}/Baseline_{680nm}}{Pulse_{900nm}/Baseline_{900nm}}$$

Empirical fitting procedures establish relationships between R and SpO_2. In the case of this study, the fit coefficients were determined using reference SpO2 values generated from data originating from patients post-surgery with the greatest range of SpO_2 in their medical record while the devices were mounted.

Multiwavelength delay

Calculations of MW delay were performed on windows of 5 s of pulsatile signals with the same 0.5–5 Hz bandwidth from all 6 available wavelengths. Six wavelengths were used as they are the maximum allowed in a single integration cycle on the multispectral photodiode, maximizing sample rate. The bandpassed waveforms were normalized and PCA with two output dimensions was performed on the matrix with all wavelengths and separately on a subset of this matrix consisting of only near-surface interacting wavelengths (blue-green). The PCA weights were calculated uniquely on each window to prevent motion artefacts and pulse morphology changes from other sections of the dataset from influencing local processes. Following approaches similar to those reported previously[44] and visually described in Supplementary Fig. 3, the first component of the PCA with all the wavelengths was theorized to consist of a superposition of arterial and capillary-type pulsations, while the first component of the PCA with only near-surface wavelengths was considered to contain only capillary components. A signal consisting of primarily arterial pulsation followed from subtraction of the latter from the former. The capillary and arterial pulse waveforms were then compared using a fractional delay estimation algorithm based on fast Fourier transform and subsample phase fitting to estimate the delay between the two signals throughout the waveform at a high precision. The second principal component from the near-surface PCA was extracted to develop signal quality indices based on statistical analysis of those generally non-pulsatile components.

Supplementary Material

Refer to Web version on PubMed Central for supplementary material.

Acknowledgements

We thank M. Banet and J. Martucci for their invaluable expertise and insights throughout the development and execution of this project. A.T. discloses support for the research described in this study from the National Heart, Lung and Blood Institute of the National Institutes of Health (grant number F30HL157066). The work was also supported in part by the National Center for Advancing Translational Sciences (NCATS; grant UM1TR004407 to J.P.).

Data availability

The data used for the training of the classification model are presented in its entirety in Fig. 5 and are available from the corresponding authors on reasonable request and Institutional Review Board approval.

References

1. Heidenreich PA et al. 2022 AHA/ACC/HFSA guideline for the management of heart failure: a report of the American College of Cardiology/American Heart Association Joint Committee on Clinical Practice Guidelines. J. Am. Coll. Cardiol. 79, e263–e421 (2022). [PubMed: 35379503]
2. January CT et al. 2019 AHA/ACC/HRS focused update of the 2014 AHA/ACC/HRS guideline for the management of patients with atrial fibrillation: a report of the American College of Cardiology/American Heart Association Task Force on Clinical Practice Guidelines and the Heart Rhythm Society in Collaboration With the Society of Thoracic Surgeons. Circulation 140, e125–e151 (2019). [PubMed: 30686041]
3. Truby LK & Rogers JG Advanced heart failure: epidemiology, diagnosis, and therapeutic approaches. Heart Fail. 8, 523–536 (2020).
4. Pinsky MR & Payen D Functional hemodynamic monitoring. Crit. Care 9, 566–572 (2005). [PubMed: 16356240]
5. Teboul JL et al. Less invasive hemodynamic monitoring in critically ill patients. Intensive Care Med. 42, 1350–1359 (2016). [PubMed: 27155605]
6. Cotter G et al. The role of cardiac power and systemic vascular resistance in the pathophysiology and diagnosis of patients with acute congestive heart failure. Eur. J. Heart Fail. 5, 443–451 (2003). [PubMed: 12921805]
7. Delong C & Sharma S Physiology, Peripheral Vascular Resistance (StatPearls Publishing, 2022).
8. Keville MP et al. Arterial or cuff pressure: clinical predictors among patients in shock in a critical care resuscitation unit. Am. J. Emerg. Med. 46, 109–115 (2021). [PubMed: 33744746]
9. Tran QK et al. Discrepancy between invasive and noninvasive blood pressure measurements in patients with sepsis by vasopressor status. West. J. Emerg. Med. 23, 358–367 (2022). [PubMed: 35679499]
10. Chen Y et al. Right heart catheterization-related complications: a review of the literature and best practices. Cardiol. Rev. 28, 36–41 (2020). [PubMed: 31804291]
11. Desai AS et al. Ambulatory hemodynamic monitoring reduces heart failure hospitalizations in 'real-world' clinical practice. J. Am. Coll. Cardiol. 69, 2357–2365 (2017). [PubMed: 28330751]
12. Abraham J et al. Association of ambulatory hemodynamic monitoring of heart failure with clinical outcomes in a concurrent matched cohort analysis. JAMA Cardiol. 4, 556–563 (2019). [PubMed: 31090869]
13. Malasinghe LP, Ramzan N & Dahal K Remote patient monitoring: a comprehensive study. J. Ambient Intell. Humaniz. Comput. 10, 57–76 (2019).
14. Noah B et al. Impact of remote patient monitoring on clinical outcomes: an updated meta-analysis of randomized controlled trials. npj Digital Med. 1, 20172 (2018).
15. Yetisen AK et al. Wearables in medicine. Adv. Mater. 30, 1706910 (2018). [PubMed: 29893068]
16. Olmedo-Aguirre JO et al. Remote healthcare for elderly people using wearables: a review. Biosensors 12, 73 (2022). [PubMed: 35200334]
17. Bayoumy K et al. Smart wearable devices in cardiovascular care: where we are and how to move forward. Nat. Rev. Cardiol. 18, 581–599 (2021). [PubMed: 33664502]
18. Pevnick JM, Birkeland K, Zimmer R, Elad Y & Kedan I Wearable technology for cardiology: an update and framework for the future. Trends Cardiovasc. Med. 28, 144–150 (2018). [PubMed: 28818431]
19. Prieto-Avalos G et al. Wearable devices for physical monitoring of heart: a review. Biosensors 12, 292 (2022). [PubMed: 35624593]

20. Huhn S et al. The impact of wearable technologies in health research: scoping review. JMIR Mhealth Uhealth 10, e34384 (2022). [PubMed: 35076409]
21. Boubouchairopoulou N, Ntineri A, Kollias A, Destounis A & Stergiou GS Blood pressure variability assessed by office, home, and ambulatory measurements: comparison, agreement, and determinants. Hypertens. Res. 44, 1617–1624 (2021). [PubMed: 34599293]
22. Stergiou GS et al. Hypertension evaluation of the accuracy of cuffless blood pressure measurement devices: challenges and proposals. Hypertension 78, 1161–1167 (2021). [PubMed: 34510915]
23. Stergiou GS et al. Cuffless blood pressure measuring devices: review and statement by the European Society of Hypertension Working Group on Blood Pressure Monitoring and Cardiovascular Variability. J. Hypertens. 40, 1449–1460 (2022). [PubMed: 35708294]
24. Schutte AE, Kollias A & Stergiou GS Blood pressure and its variability: classic and novel measurement techniques. Nat. Rev. Cardiol. 19, 643–654 (2022). [PubMed: 35440738]
25. Stergiou GS et al. Methodology and technology for peripheral and central blood pressure and blood pressure variability measurement: current status and future directions – position statement of the European Society of Hypertension Working Group on blood pressure monitoring and cardiovascular variability. J. Hypertens. 34, 1665–1677 (2016). [PubMed: 27214089]
26. Ma Y et al. Relation between blood pressure and pulse wave velocity for human arteries. Proc. Natl Acad. Sci. USA 115, 11144–11149 (2018). [PubMed: 30322935]
27. Mukkamala R et al. Towards ubiquitous blood pressure monitoring via pulse transit time: theory and practice HHS public access. IEEE Trans. Biomed. Eng. 62, 1879–1901 (2015). [PubMed: 26057530]
28. Wibmer T et al. Blood pressure monitoring during exercise: comparison of pulse transit time and volume clamp methods. Blood Press. 24, 353–360 (2015). [PubMed: 26286887]
29. Finnegan E et al. Pulse arrival time as a surrogate of blood pressure. Sci. Rep. 11, 22767 (2021). [PubMed: 34815419]
30. Proenç J, Muehlsteff J, Aubert X & Carvalho P Is pulse transit time a good indicator of blood pressure changes during short physical exercise in a young population? Annu. Int. Conf. IEEE Eng. Med. Biol. Soc. 2010, 598–601 (2010). [PubMed: 21096104]
31. Kounalakis SN & Geladas ND The role of pulse transit time as an index of arterial stiffness during exercise. Cardiovasc. Eng. 9, 92–97 (2009). [PubMed: 19657732]
32. Polónia J, Barbosa L, Silva JA & Maldonado J Different influences on central and peripheral pulse pressure, aortic wave reflections and pulse wave velocity of three different types of antihypertensive drugs. Rev. Port. Cardiol. 22, 1485–1492 (2003). [PubMed: 15008064]
33. Kelly RP, Millasseau SC, Ritter JM & Chowienczyk PJ Vasoactive drugs influence aortic augmentation index independently of pulse-wave velocity in healthy men. Hypertension 37, 1429–1433 (2001). [PubMed: 11408390]
34. Borner A, Murray K, Trotter C & Pearson J Baseline aortic pulse wave velocity is associated with central and peripheral pressor responses during the cold pressor test in healthy subjects. Physiol. Rep. 5, e13357 (2017). [PubMed: 28733312]
35. Elias SO & Ajayi RE Effect of sympathetic autonomic stress from the cold pressor test on left ventricular function in young healthy adults. Physiol. Rep. 7, e13985 (2019). [PubMed: 30659769]
36. Parati G, Stergiou GS, Dolan E & Bilo G Blood pressure variability: clinical relevance and application. J. Clin. Hypertens. 20, 1133–1137 (2018).
37. Lantelme P, Mestre C, Lievre M, Gressard A & Milon H Heart rate: an important confounder of pulse wave velocity assessment. Hypertension 39, 1083–1087 (2002). [PubMed: 12052846]
38. Papaioannou TG et al. The influence of resting heart rate on pulse wave velocity measurement is mediated by blood pressure and depends on aortic stiffness levels: insights from the Corinthia study. Physiol. Meas. 40, 055005 (2019). [PubMed: 30952147]
39. Sherwood A et al. Methodological guidelines for impedance cardiography. Psychophysiology 27, 1–23 (1990). [PubMed: 2187214]
40. Kouz K, Scheeren TWL, de Backer D & Saugel B Pulse wave analysis to estimate cardiac output. Anesthesiology 134, 119–126 (2021). [PubMed: 32914174]
41. Hametner B & Wassertheurer S Pulse waveform analysis: is it ready for prime time? Curr. Hypertens. Rep. 19, 1–7 (2017). [PubMed: 28083801]

42. Liu J et al. Multi-wavelength photoplethysmography method for skin arterial pulse extraction. Biomed. Opt. Express 7, 4313 (2016). [PubMed: 27867733]
43. Liu J et al. Multi-wavelength photoplethysmography enabling continuous blood pressure measurement with compact wearable electronics. IEEE Trans. Biomed. Eng. 66, 1514–1525 (2019). [PubMed: 30307851]
44. Liu J et al. PCA-based multi-wavelength photoplethysmography algorithm for cuffless blood pressure measurement on elderly subjects. IEEE J. Biomed. Health Inf. 25, 663–673 (2021).
45. Spigulis J, Gailite L, Lihachev A & Erts R Simultaneous recording of skin blood pulsations at different vascular depths by multiwavelength photoplethysmography. Appl. Opt. 56, 1754–1759 (2007).
46. Aidar FJ et al. Can post-exercise hemodynamic response be influenced by different recovery methods in paraplegic sportsmen? Int. J. Environ. Res. Public Health 19, 1772 (2022). [PubMed: 35162794]
47. Francisco MA et al. Hemodynamics of postexercise versus post-hot water immersion recovery. J. Appl. Physiol. 130, 1362–1372 (2021). [PubMed: 33630675]
48. Churchill TW The impact of exercise and athletic training on vascular structure and function. Curr. Treat. Options Cardiovasc. Med. 22, 1–11 (2020). [PubMed: 31938936]
49. Bauer P et al. Blood pressure response and vascular function of professional athletes and controls. Sports Med. Int. Open 5, E45–E52 (2021). [PubMed: 33889714]
50. McDuff D et al. Non-contact imaging of peripheral hemodynamics during cognitive and psychological stressors. Sci. Rep. 10, 1–13 (2020). [PubMed: 31913322]
51. Chung HU et al. Skin-interfaced biosensors for advanced wireless physiological monitoring in neonatal and pediatric intensive-care units. Nat. Med. 26, 418–429 (2020). [PubMed: 32161411]
52. Lee KH et al. Mechano-acoustic sensing of physiological processes and body motions via a soft wireless device placed at the suprasternal notch. Nat. Biomed. Eng. 4, 148–158 (2020). [PubMed: 31768002]
53. Finlayson L et al. Depth penetration of light into skin as a function of wavelength from 200 to 1000 nm. Photochem. Photobiol. 98, 974–981 (2022). [PubMed: 34699624]
54. Rwei AY et al. A wireless, skin-interfaced biosensor for cerebral hemodynamic monitoring in pediatric care. Proc. Natl Acad. Sci. USA 117, 31674–31684 (2020). [PubMed: 33257558]
55. Nishimura RA & Tajik AJ The Valsalva maneuver and response revisited. Mayo Clin. Proc. 61, 211–217 (1986). [PubMed: 3511334]
56. Bennett T, Hosking DJ & Hampton JR Vasomotor responses to the Valsalva maneuver in normal subjects and in patients with diabetes mellitus. Br. Heart J. 42, 422–428 (1979). [PubMed: 508473]
57. Awad AA et al. Different responses of ear and finger pulse oximeter wave form to cold pressor test. Anesth. Analg. 92, 1483–1486 (2001). [PubMed: 11375830]
58. Lovallo W The cold pressor test and autonomic function: a review and integration. Psychophysiology 12, 268–282 (1975). [PubMed: 1153632]
59. Heistad DD, Abboud FM & Eckstein JW Vasoconstrictor response to simulated diving in man. J. Appl. Physiol. 25, 542–549 (1968). [PubMed: 5687360]
60. Kellogg DL, Crandall CG, Liu Y, Charkoudian N & Johnson JM Nitric oxide and cutaneous active vasodilation during heat stress in humans. J. Appl. Physiol. 85, 824–829 (1998). [PubMed: 9729553]
61. Kim MY et al. Acute reduction of pulse wave velocity after sauna in adults in a community. J. Korean Acad. Fam. Med. 27, 384–390(2006).
62. Lee E et al. Sauna exposure leads to improved arterial compliance: findings from a non-randomised experimental study. Eur. J. Prev. Cardiol. 25, 130–138 (2018). [PubMed: 29048215]
63. Laukkanen T et al. Acute effects of sauna bathing on cardiovascular function. J. Hum. Hypertens. 32, 129–138 (2017). [PubMed: 29269746]
64. Teixeira L, Ritti-Dias RM, Tinucci T, Mion D & de Moraes Forjaz CL Post-concurrent exercise hemodynamics and cardiac autonomic modulation. Eur. J. Appl. Physiol. 111, 2069–2078 (2011). [PubMed: 21259026]

65. Vatner SF & Pagani M Cardiovascular adjustments to exercise: hemodynamics and mechanisms. Prog. Cardiovasc. Dis. 19, 91–108 (1976). [PubMed: 790460]
66. Desebbe O et al. Control of postoperative hypotension using a closed-loop system for norepinephrine infusion in patients after cardiac surgery: a randomized trial. Anesth. Analg. 134, 964–973 (2022). [PubMed: 35061635]
67. Klabunde RE Cardiovascular Physiology Concepts (Wolters Kluwer, Lippincott Williams & Wilkins, 2021).
68. Hofmann H, Wickham H & Kafadar K Letter-value plots: boxplots for large data. J. Comput. Graph. Stat. 26, 469–477 (2017).
69. Brunner E & Munzel U Rank-score tests in factorial designs with repeated measures. J. Multivar. Anal. 70, 286–317 (1999).
70. Mitchell LA, MacDonald RAR & Brodie EE Temperature and the cold pressor test. J. Pain 5, 233–237 (2004). [PubMed: 15162346]
71. Reddy S Explainability and artificial intelligence in medicine. Lancet Digit. Health 4, e214–e215 (2022). [PubMed: 35337639]
72. Lundberg SM, Allen PG & Lee S-I A unified approach to interpreting model predictions. Adv. Neural Inf. Process. Syst. 30, 4765–4774 (2017).
73. Newlin DB & Levenson RW Pre-ejection period: measuring beta-adrenergic influences upon the heart. Psychophysiology 16, 546–552 (1979). [PubMed: 229507]
74. Garrard CL, Weissler AM & Dodge HT The relationship of alterations in systolic time intervals to ejection fraction in patients with cardiac disease. Circulation 42, 455–462 (1970). [PubMed: 5451230]
75. Harris CR et al. Array programming with NumPy. Nature 585, 357–362 (2020). [PubMed: 32939066]
76. Virtanen P et al. SciPy 1.0: fundamental algorithms for scientific computing in Python. Nat. Methods 17, 261–272 (2020). [PubMed: 32015543]
77. McKinney W Data structures for statistical computing in Python. In Proc. 9th Python in Science Conf. (eds van der Walt S & Millman KJ) 56–61 (2010).
78. Pedregosa F et al. Scikit-learn: machine learning in Python. J. Mach. Learn. Res. 12, 2825–2830 (2011).
79. Hunter JD Matplotlib: a 2D graphics environment. Comput. Sci. Eng. 9, 90–95 (2007).
80. Waskom M seaborn: statistical data visualization. J. OpenSource Softw. 6, 3021 (2021).
81. Maeda Y, Sekine M & Tamura T The advantages of wearable green reflected photoplethysmography. J. Med. Syst. 35, 829–834 (2011). [PubMed: 20703690]
82. Lee J et al. Comparison between red, green and blue light reflection photoplethysmography for heart rate monitoring during motion. Annu. Int. Conf. IEEE Eng. Med. Biol. Soc. 2013, 1724–1727 (2013). [PubMed: 24110039]
83. Scholkmann F, Boss J & Wolf M An efficient algorithm for automatic peak detection in noisy periodic and quasi-periodic signals. Algorithms 5, 588–603 (2012).

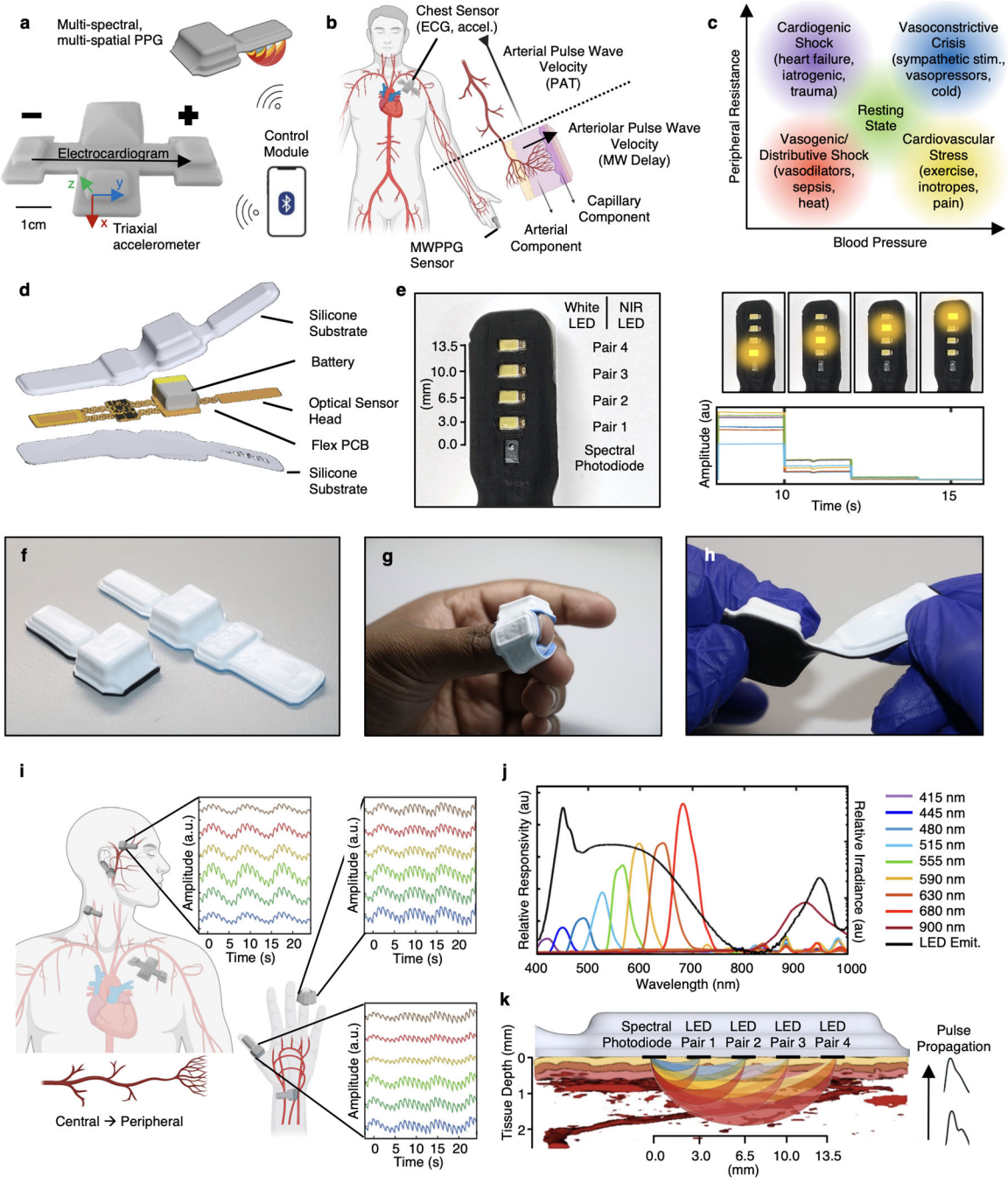

Fig. 1 |. Combined hemodynamic sensor concepts and devices overview.

a, The sensor system consists of a peripherally mounted sensor capable of MWPPG measurements, and a chest-mounted sensor capable of ECG and triaxial accelerometry. Both sensors are coordinated wirelessly via a Bluetooth-enabled control module. **b**, Time-synchronized measurement of ECG and PPG enables estimation of systemic blood pressure via arterial pulse wave velocity, while MWPPG enables quantification of local/ peripheral arteriolar states. **c**, Combining these hemodynamic sensors enables differentiation of hemodynamic states in dimensions of clinically pertinent hemodynamic parameters of

blood pressure and vascular resistance. **d**, Exploded rendering of the multispectral device with silicone encapsulation layers, fPCB consisting of four islands separated via flexible serpentine interconnects and support circuitry. **e**, Left: bottom view of the multiwavelength sensor with multiple pairs of individually controllable broadband and NIR LEDs. Source-detector distances are 3 mm, 6.5 mm, 10 mm and 13.5 mm. Right: time-sequential LED sequencing allows for spatially resolved spectroscopy useful in tissue oximetry. **f**, Side-by-side views of two different form factors achievable by folding the fPCB. **g**, Device placement as a finger wrap. **h**, Mechanical twisting of the peripheral multiwavelength device in its short form. **i**, Diagram indicating various possible placements of the devices and associated normalized waveforms, offset for clarity, from central and peripheral locations, and with both arterial-dominated or capillary-dominated vascular beds (more detail in Supplementary Fig. 2). Obtained during deep breathing exercises, the signal contains both low-frequency oscillations due to respiration and high-frequency oscillations due to the cardiac cycle. **j**, Monochromator scan of an encapsulated device showing relative responsivity (left axis) at 9 different wavelengths throughout the visible and NIR ranges as well as LED pair emittance spectrum (black, right axis). **k**, Diagram of the measurement principles showing simultaneous wavelength- and distance-based light paths through a photoacoustic tomography rendering of real human skin. Portions of this figure were created with BioRender.com.

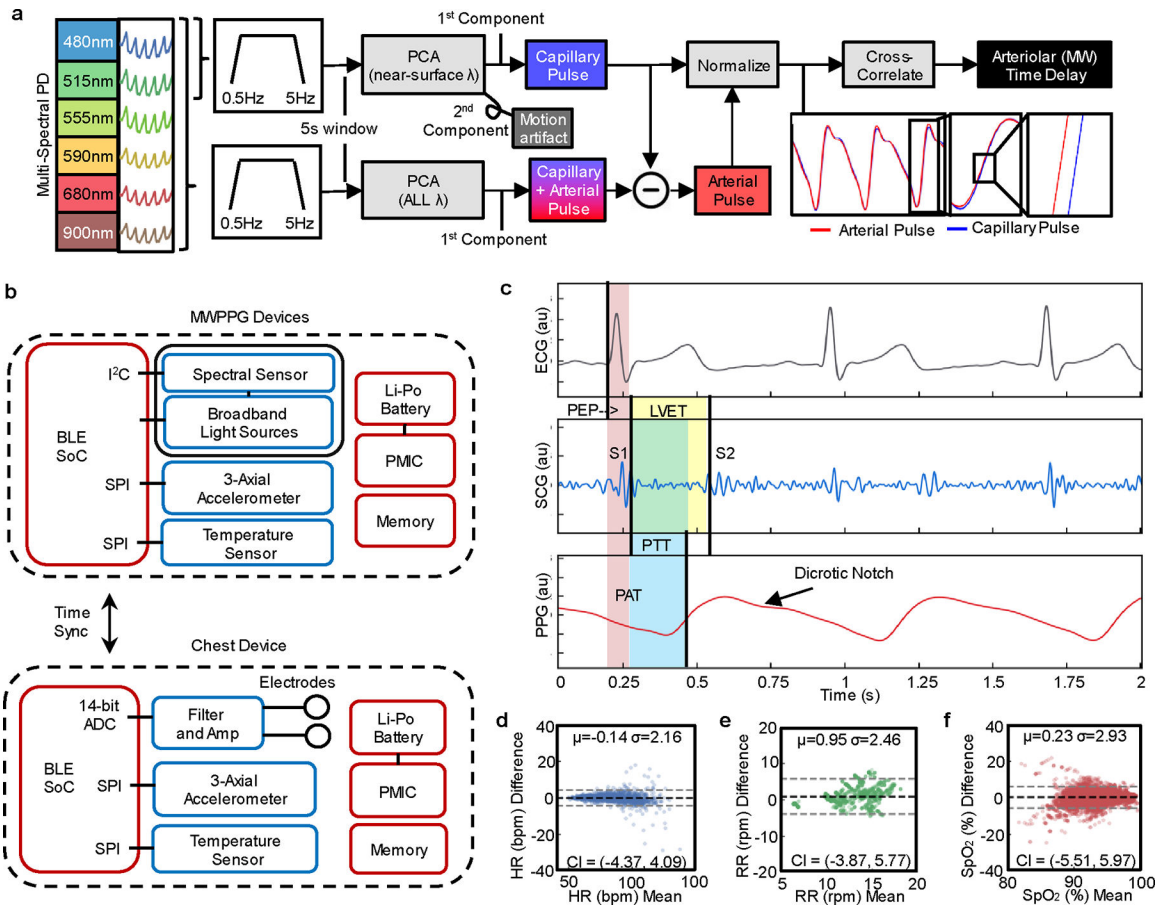

Fig. 2 |. Combined hemodynamic sensor system and measurements.

a, Data analysis pipeline for extraction of arteriolar pulse transit time, extracting capillary and arterial pulsations from six discrete wavelength channels and employing normalized subsampled cross-correlation to extract arteriolar (MW) time delay. **b**, Block diagram of the sensors and key components enabling cross-body, central-vs-peripheral measurements of different modalities with BLE wireless communication. PMIC, power management integrated circuitry; I2C or SPI, serial peripheral interface; ADC, analogue–digital converter. **c**, Example of time-synchronized sensor waveforms from the ECG, *z*-axis accelerometer SCG and PPG, with signal features and key physiological time intervals of hemodynamic relevance indicated: first mitral/tricuspid heart sound (S1), second aortic/pulmonic heart sound (S2), PEP, LVET, PAT, PTT. **d**–**f**, Bland–Altman plots with bias (black dashed line) and ±1.96 s.d.s (dashed grey lines, confidence intervals (CI)) for conventional vitals measurements of HR (**d**), RR (**e**) and SpO_2 (**f**) against references: Finapres pulse rate was used for healthy participants; HR, RR and SpO_2 references were extracted from the electronic medical record of all patients.

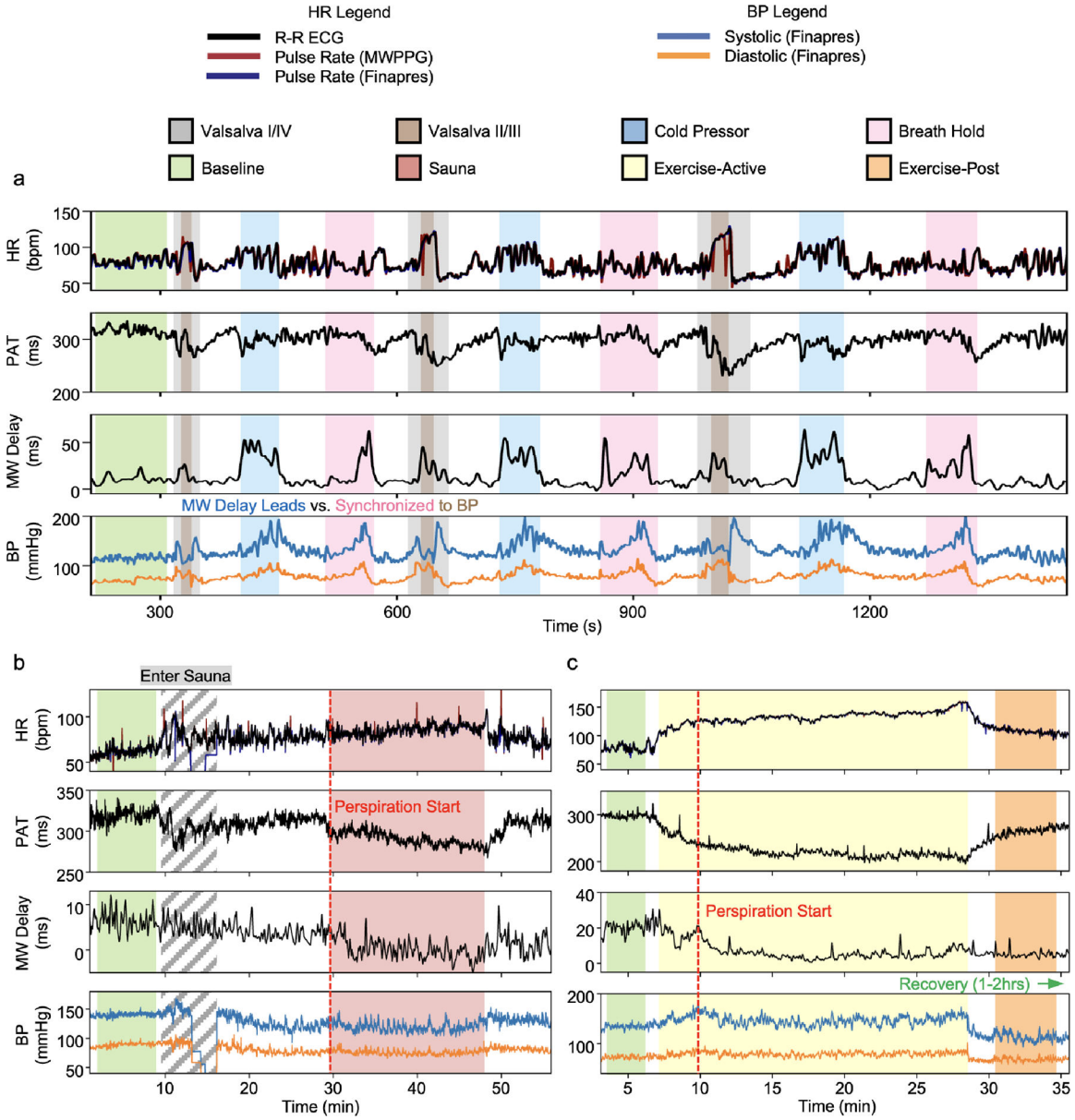

Fig. 3 |. Representative hemodynamic studies on healthy individuals.

a, Short-term interleaved pressor tests, cycling through Valsalva maneuver, cold pressor test and breath holding. A consistent rise in MW delay signal during ice bath exposure precedes a complementary rise in BP, indicating that MW delay is measuring a driving force inducing BP change. Conversely, alignment of MW delay increase with BP in Valsalva phases II/III and breath holds indicates measurement of the reverse scenario—a compensatory, sympathetic vasoactive response to stimulus. **b**, A 20-min heat exposure challenge via personal sauna. BP drops from baseline associated with a rise in HR, suggesting vasodilative hypotension. Note the loss of Finapres data during sauna entry, necessary due to disconnection of the wired system to pass the hand through a hole, while the wireless sensors experience no such limitation. Contrary to theory, PAT drops during this period, especially after profuse perspiration begins. MW delay exhibits a small drop during

heat exposure, which is partially reversed upon exiting the chamber. **c**, A 20-min exercise bike session, showing drastic change in PAT mirroring the HR which returns to baseline. MW delay begins to drop only after the patient begins vasodilating, which occurs at the peak BP a few minutes after exercise starts. The delay remains low after exercise is complete and BP is still low despite the PAT return to baseline levels.

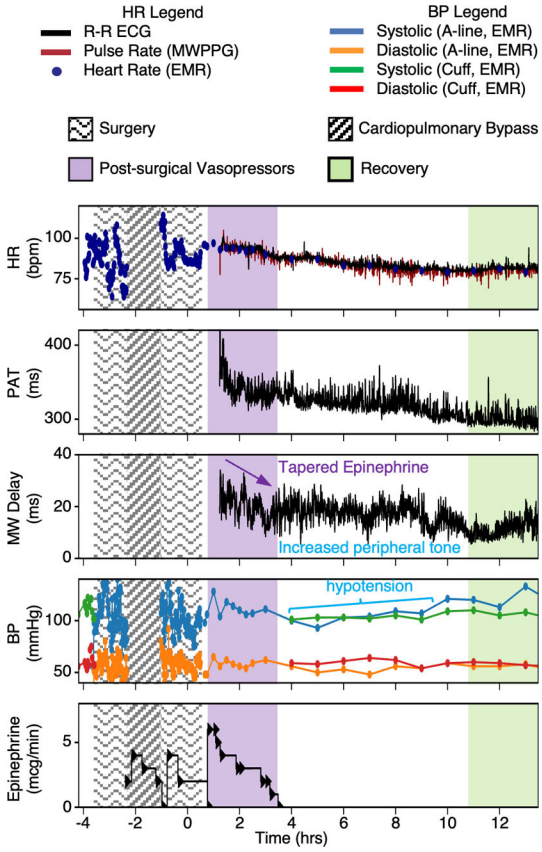

Fig. 4 |. Post-surgical monitoring.

A patient monitored for a 12-h period post mitral valve repair was given intravenous epinephrine in response to post- operative hypotension noted in the electronic medical record (EMR). Hour 0 corresponds to the start of surgical wound closure. Intravenous epinephrine was started after initial rooming and assessment, and devices were placed shortly afterwards. While the medication was tapered after 3 h, MW delay remained high in the setting of hypotension, suggesting elevated peripheral vascular tone. This lasted until the patient's BP recovered and the patient was able to feed, 10 h after surgery completion.

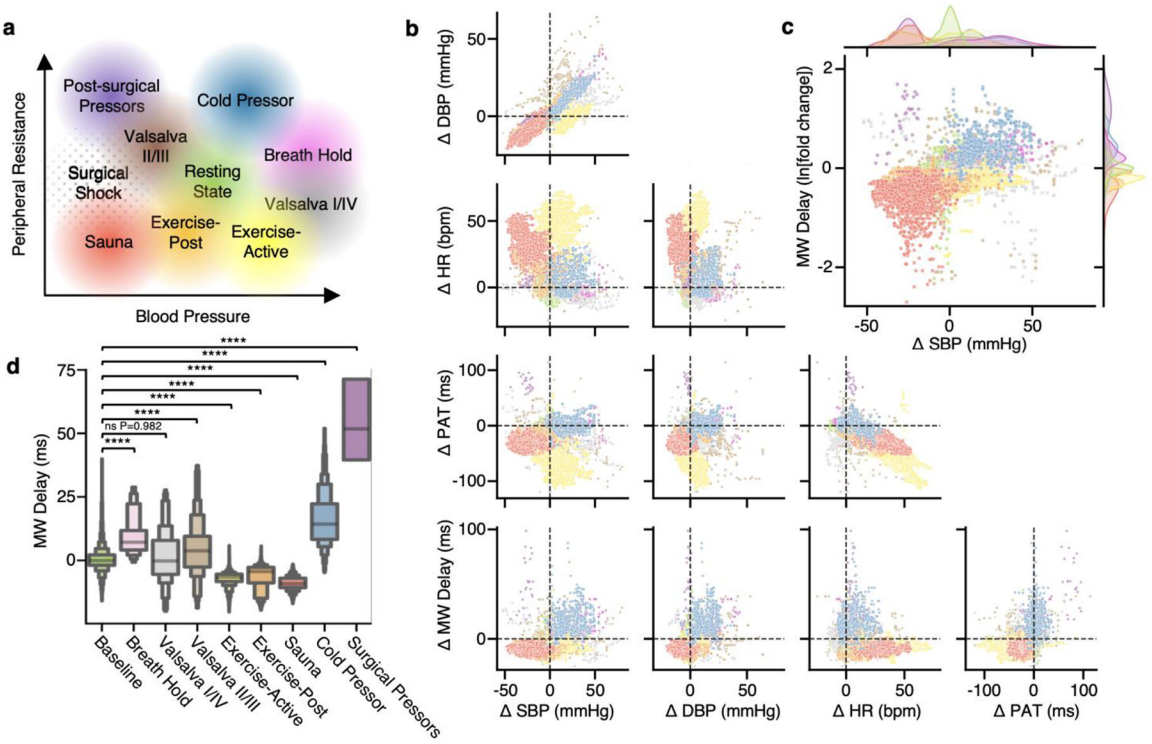

Fig. 5 |. Hemodynamic measurement scatterplots.

a, Theoretical plot between peripheral resistance and BP, indicating hypothesized relationships of different hemodynamic stimuli. **b**, Baseline-subtracted scatterplots between HR (bpm), PAT (ms), MW delay (ms) and systolic/diastolic BP (mmHg), with each sample color coded by stimulus as in **a**. To control for inter-participant variability, the median of the baseline state, indicated by crosshairs, is subtracted from each datapoint. **c**, Scatterplot of the MW delay fold change on a logarithmic axis against BP, showcasing separation of stimuli into groupings in similar positions as in **a**, with kernel density estimates of distributions of these quantities outside each axis. Note the overlap of sauna and surgical pressor distributions on the BP axis, indicating that two very different states are not adequately separable using BP alone, but begin to be distinguished with the addition of MW delay. **d**, Letter-value plots of MW delay measurements during each hemodynamic state. In letter-value plots, each progressively smaller pair of boxes around the center value (median) represents a power of 2 smaller fraction of the data points, such as fourths, eighths, sixteenths and so on. Brunner–Munzel tests between each stimulus and the baseline distribution; NS, not significant, **** $P < 0.0001$.

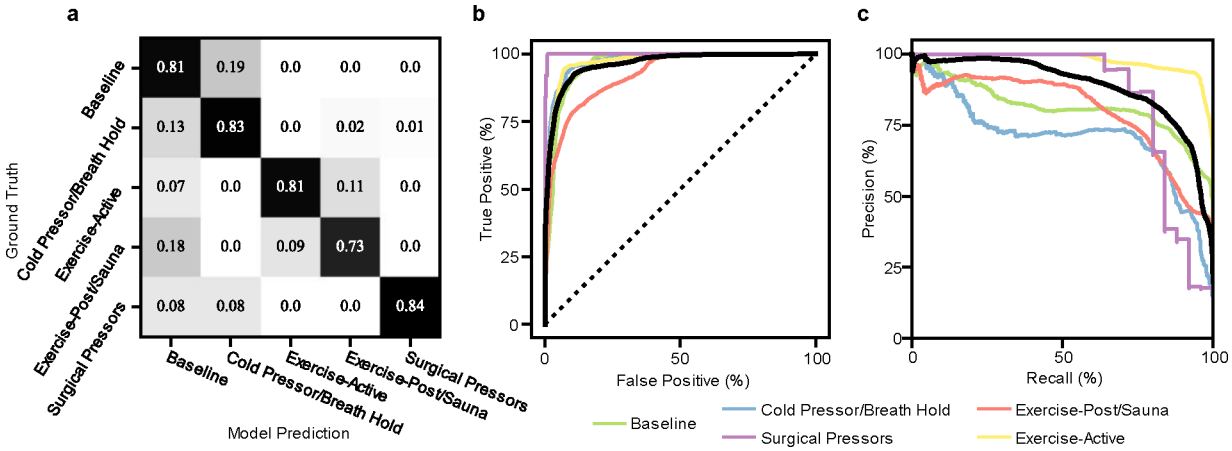

Fig. 6 |. Hemodynamic classification.

a, Confusion matrix of model predictions, grouped by hemodynamic condition (quadrant on BP vs SVR axis). **b**, **c**, Receiver operating characteristic curves (**b**) and precision-recall curves (**c**) for all hemodynamic state predictions (one vs all) colored by the quadrants outlined in Fig. 1c, and highlighted micro-average curve in black. Area under the curve values for receiver operating characteristic curves are: baseline = 0.96, exercise = 0.98, sauna = 0.93, cold pressor/breath hold = 0.98, surgical pressors = 1.0. Area under the curve values for precision-recall curves are (baseline = 0.82, exercise = 0.98, sauna = 0.80, cold pressor/breath hold = 0.73, surgical pressors = 0.93).